



On-chip optical parametric oscillation into the visible: generating red, orange, yellow, and green from a near-infrared pump

XIYUAN LU,^{1,2,5} GREGORY MOILLE,^{1,3}  ASHUTOSH RAO,^{1,4} DARON A. WESTLY,¹ AND KARTIK SRINIVASAN^{1,3,*} 

¹Microsystems and Nanotechnology Division, Physical Measurement Laboratory, National Institute of Standards and Technology, Gaithersburg, Maryland 20899, USA

²Institute for Research in Electronics and Applied Physics and Maryland NanoCenter, University of Maryland, College Park, Maryland 20742, USA

³Joint Quantum Institute, NIST/University of Maryland, College Park, Maryland 20742, USA

⁴Department of Chemistry and Biochemistry, University of Maryland, College Park, Maryland 20742, USA

⁵e-mail: xiyuan.lu@nist.gov

*Corresponding author: kartik.srinivasan@nist.gov

Received 27 March 2020; revised 25 August 2020; accepted 1 September 2020 (Doc. ID 393810); published 12 October 2020

The on-chip generation of coherent, single-frequency laser light that can be tuned across the visible spectrum would help enable a variety of applications in spectroscopy, metrology, and quantum science. Recently, third-order optical parametric oscillation (OPO) in a microresonator has shown great promise as an efficient and scalable approach toward this end. However, considering visible light generation, so far only red light at <420 THz (near the edge of the visible band) has been reported. In this work, we overcome strong material dispersion at visible wavelengths and demonstrate on-chip OPO in a Si₃N₄ microresonator covering >130 THz of the visible spectrum, including red, orange, yellow, and green wavelengths. In particular, using an input pump laser that is scanned 5 THz in the near-infrared from 386 THz to 391 THz, the OPO output signal is tuned from the near-infrared at 395 THz to the visible at 528 THz, while the OPO output idler is tuned from the near-infrared at 378 THz to the infrared at 254 THz. The widest signal-idler separation of 274 THz is more than an octave in span and is the widest demonstrated for a nanophotonic OPO to date. More generally, our work shows how nonlinear nanophotonics can transform light from readily accessible compact near-infrared lasers to targeted visible wavelengths of interest. © 2020 Optical Society of America under the terms of the [OSA Open Access Publishing Agreement](#)

<https://doi.org/10.1364/OPTICA.393810>

1. INTRODUCTION

On-chip generation of coherent visible light is important for scalable manufacturing and field-level deployment of many applications in spectroscopy, metrology, and quantum optics. For example, many wavelength references [1] and optical clocks [2] are based on visible lasers stabilized to atomic systems. Moreover, many quantum systems suitable for local storage and manipulation of quantum information, including trapped ions, atoms, and spins in crystals, have optical transitions that require visible pump lasers for operation [3]. A direct approach is to develop on-chip lasers based on III-V semiconductors (e.g., indium gallium nitride lasers [4]), but spectral coverage is typically limited by the available gain media. Achieving spectral coverage via direct optical transitions over a wide range of wavelengths is challenging, and integrating such a laser into a mature photonic integrated circuit platform is also nontrivial.

Nonlinear optics is another route to visible light generation. While optical harmonic generation enables access to visible wavelengths via a near-infrared pump, the output frequency tuning

range is limited to a small multiple of the input frequency tuning range. In contrast, optical parametric oscillation (OPO) provides a mechanism by which output light with wide spectral coverage can be obtained using only limited tuning of a single pump laser [5,6]. Over the past few decades, table-top OPO has been extensively studied for visible light generation [7], and has been a major workhorse for laboratory purposes. Such table-top OPO provides a versatile source of high-power tunable laser light, but is also bulky, expensive, and lacks the miniaturization and scalability for field-level deployment in many applications.

On-chip OPO based on both the second-order ($\chi^{(2)}$) and third-order ($\chi^{(3)}$) nonlinearity has been intensely studied in microphotonic and nanophotonic resonators. While both processes can be successful, we note that the pump laser requirements are very different. For $\chi^{(2)}$ OPO, the energy conservation criterion requires $\nu_p = \nu_s + \nu_i$, where p, s, and i represent the pump, signal, and idler, respectively. As a result, generation of a visible wavelength signal will require a pump laser in the blue to ultraviolet region (depending on how short an output wavelength

is desired). In contrast, for $\chi^{(3)}$ OPO, the energy conservation criterion is $2\nu_p = \nu_s + \nu_i$. Because two pump photons now contribute to the process, visible wavelength output is accessible from a near-infrared pump laser. Such lasers are commercially available in compact forms, including distributed feedback (DFB) and distributed Bragg reflector (DBR) geometries.

In this work, we demonstrate widely separated OPO based on the third-order nonlinearity in a silicon nitride (Si_3N_4) microring [Fig. 1(a)]. Our OPO devices address $\approx 34\%$ (130 THz) of the

visible spectrum, including red, orange, yellow, and green colors, through a small change in the pump laser frequency [Fig. 1(b)]. Our approach enables octave-spanning OPO to be observed, with a 527.8 THz (568.4 nm) signal in the green and a 254.1 THz (1181 nm) idler in the infrared. To the best of our knowledge, the corresponding span of 273.7 THz is the widest on-chip OPO reported so far: it is >40 THz larger than the previous record [8] set for an infrared OPO, despite the substantial increase in material dispersion at visible wavelengths [Fig. 1(c)]. We further show that

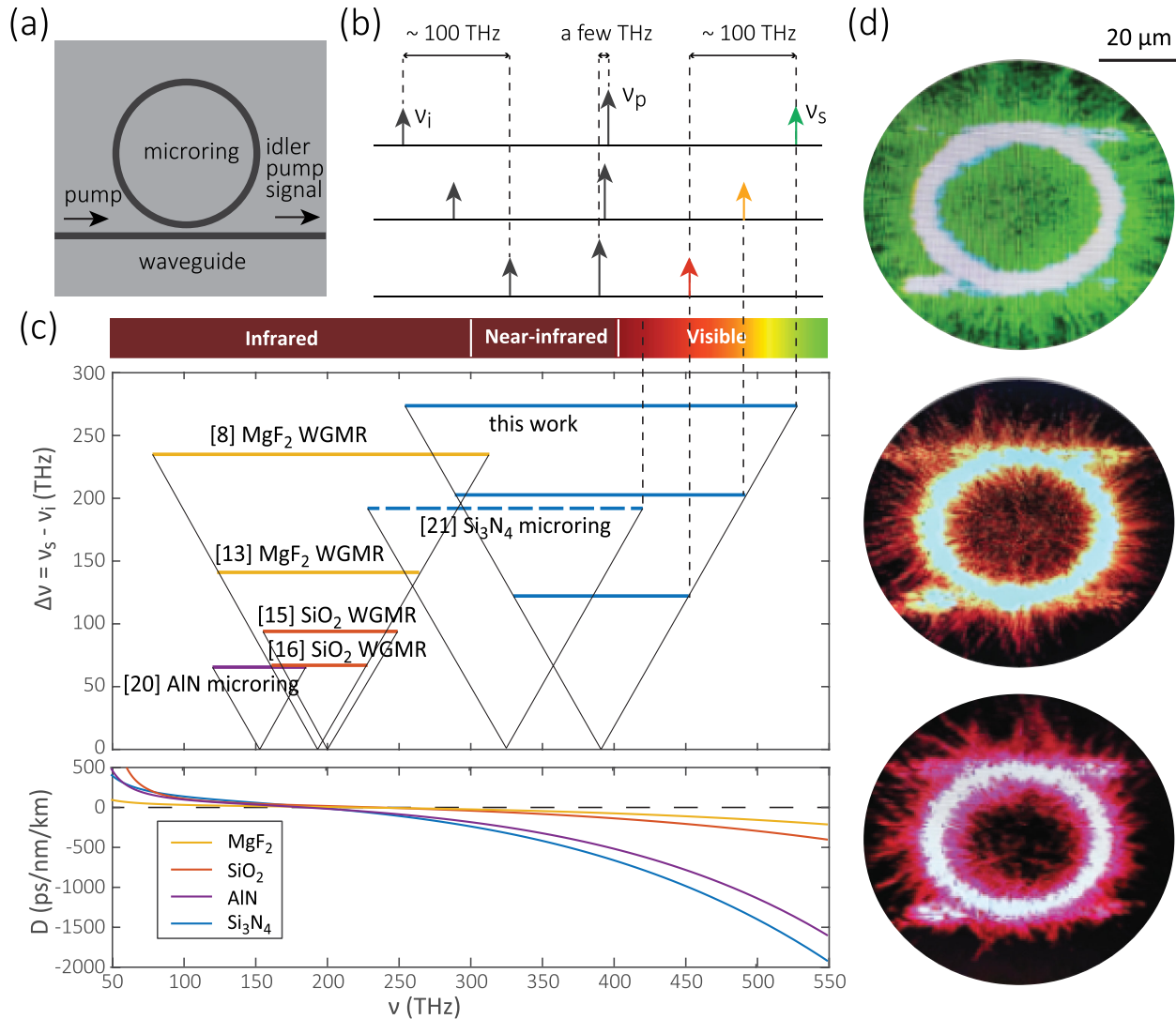


Fig. 1. OPO transforms a near-infrared pump into visible wavelength light. (a) Device and (b) scheme of the OPO process to generate signal and idler in the visible and infrared, respectively, using a pump in the near-infrared. When the pump shifts by only a few THz, the OPO outputs shift by ≈ 100 THz. This advantage makes OPO unique for light generation over broad spectral bands. (c) Comparison (top) of OPO with widely separated signal and idler in miniaturized/on-chip photonic devices. Most of these works are pumped by infrared lasers either at ≈ 193.5 THz (1.55 μm) for MgF₂ and SiO₂ whispering gallery mode resonators (WGMRs) or at ≈ 150 THz (2 μm) in an AlN microring, where the representative data with the widest span (y axis) are shown by the solid horizontal lines. A recent OPO work in Si₃N₄ uses a near-infrared pump at ≈ 330 THz (910 nm) to generate red light at the edge of the visible at ≈ 420 THz (714 nm), as shown by the dashed blue line. The contribution of the current work is to go deeper into the visible (the solid blue lines), where material dispersion is much larger (e.g., Si₃N₄ dispersion curve in blue in the bottom panel), covering from red (bottom) to green (top), using only a few THz of pump tuning around ≈ 385 THz (780 nm). In particular, the top line (corresponding to green light generation) shows the case where the OPO is octave-spanning, with idler and signal bridging infrared and green wavelengths. In Section 5, we show that the experimental result is very close to simulation (273.7 THz). (d) Top view microscope images of devices exhibiting OPO, showing the scattering of generated visible light in the red, orange, and green. These images are taken without ambient illumination, using a camera that is insensitive to the pump and generated idler wavelengths. The device is a Si₃N₄ microring with an outer radius of 25 μm . The 20 μm scale bar in the top right corner applies to all three images. Two waveguides are designed for each microring, as evident from the scattered light in the images, but only the bottom waveguide is used to effectively couple pump, signal, and idler light, as depicted in (a).

through power tuning, the visible output signal can be tuned in a finer fashion, similar to devices with larger footprints. Our work represents a major advance in the use of nonlinear nanophotonics to access desired wavelengths in the visible spectrum [Fig. 1(d)], and may have numerous applications in spectroscopy, metrology, and quantum science.

2. OPO IN MILLIMETER-TO-MICROMETER SCALE RESONATORS FOR VISIBLE LIGHT GENERATION

Before discussing our specific approach, in this section we review earlier works in using compact, monolithic resonators toward the goal of visible light generation via OPO. Ultra-high Q , millimeter-sized crystalline resonators have been a major platform for miniaturization of OPO for light generation in the visible [9–11] and infrared [8,12,13]. For example, $\chi^{(2)}$ OPO in a crystalline resonator has been used to generate red light near 700 nm through a blue pump laser at 488 nm [9], and subsequently even yellow light down to 570 nm was generated through a close-to-violet pump at 450 nm [14]. $\chi^{(3)}$ OPO in a crystalline resonator also has been used to generate light into the visible, albeit with multiple signal/idler sidebands or through cascaded OPO. For example, multiple OPO lines emanating from the pump and reaching down to the orange has been shown [10], and a broad set of parametric sidebands ranging from red to blue has been observed as a result of cascading nonlinear processes [11]. Within the infrared band, cluster combs with multiple frequency lines around the dominant OPO lines have been reported [12]. Importantly, single-pair octave-span OPO has been reported recently and is very promising for widely tuned coherent light generation [8,13], but it has not been demonstrated in the visible, where the constituent materials are more dispersive [e.g., see the dispersion curves in Fig. 1(c)]. We note that silica microresonators also have been used to generate widely separated OPO in the infrared using $\chi^{(3)}$ OPO [15], and to generate visible light using cascading nonlinear optical processes [16,17].

Nanophotonic resonators enable strong enhancement of light intensities in time and space, and make both $\chi^{(2)}$ and $\chi^{(3)}$ processes power efficient. In fact, $\chi^{(3)}$ processes can even be made comparable to $\chi^{(2)}$ processes; for example, in the case of spectral translation of signals across wide frequency separations [18]. In recent years, $\chi^{(2)}$ and $\chi^{(3)}$ nanophotonic OPO have both been reported in an aluminum nitride microcavity [19,20]. The former generates telecom output light from a near-infrared pump [19], while the latter generates an infrared output whose frequency can be tuned up to 65 THz by a 2 μ m pump laser [20].

To date, $\chi^{(2)}$ nanophotonic OPO has not been used to generate visible light, as it necessitates a high frequency pump (in the blue to ultraviolet range) that comes with challenges associated with loss and dispersion of material platforms in that range. Recently, $\chi^{(3)}$ nanophotonic OPO in a Si_3N_4 microring with widely separated outputs has been demonstrated, and red light at 420 THz (714 nm) was produced from a 325 THz (920 nm) pump [21]. While that work laid out some of the basic concepts associated with achieving widely separated $\chi^{(3)}$ OPO on-chip, several important questions were not addressed. In particular, the OPO output only reached the long wavelength edge of the visible spectrum, and the extent to which its design approach could reach wavelengths more deeply in the visible was unclear. In addition, while that work showed two base designs for OPO, there was no discussion of

whether the designs could be tailored to allow access to any wavelength of interest across a broad spectral range. These questions are fundamentally related to whether the underlying dispersion engineering is applicable at shorter wavelengths in the visible (and longer wavelengths in the infrared), where the signal and idler are much more widely separated. The fact that the constituent materials are far more dispersive at shorter wavelengths is a key challenge to overcome.

Finally, from a technological perspective, we note the benefits of the Si_3N_4 OPO platform from the perspective of potential pump laser integration. Such activities, which could include edge coupling of semiconductor gain media to the OPO chip, are being increasingly pursued in the context of microresonator frequency combs [22,23]. More intimate and scalable integration of pump lasers and Si_3N_4 nonlinear nanophotonics is also possible, and we note the substantial recent efforts on heterogeneous integration of III-V gain media on Si_3N_4 [24,25], including the demonstration of electrically injected lasing at wavelengths below 1 μ m [26]. These complementary efforts suggest that full OPO modules that flexibly convert an electrical input to a desired visible wavelength output may be possible.

3. DESIGN AND SIMULATION

The Si_3N_4 photonic platform [27] has been emphasized in several studies as being especially suitable for wideband nonlinear optics. These studies include demonstrations of octave-spanning microresonator frequency combs [28–30], frequency conversion for quantum and classical applications [18,31], and entangled photon-pair generation for quantum communication [21]. Very recently, Si_3N_4 also has been explored in the context of visible wavelength nonlinear nanophotonics [32], where close-band OPO and frequency comb generation based on a 780 nm pump laser were demonstrated.

The physical process to support widely separated OPO is cavity-enhanced degenerate four-wave mixing. To achieve such a nonlinear optical process, both the momentum and energy for the interacting cavity modes must be conserved [5,6]. For the whispering gallery modes of a microring resonator, when modes from the same mode family (e.g., the fundamental transverse-electric mode TE₁ in this work) are used, the momentum in question is in the azimuthal direction, and momentum conservation reduces to a simple equation, $m_s + m_i - 2m_p = 0$, where the subscripts s, i, p denote the signal, idler, and pump, respectively, and m is the azimuthal mode number. Energy conservation requires frequency matching, and for the energy-conserving frequencies generated by the four-wave mixing process to match the corresponding cavity modes, we need $\hat{\nu}_s + \hat{\nu}_i - 2\hat{\nu}_p$ (where $\hat{\nu}_k$ represents the center resonance frequency of k mode) to be approximately within the cavity linewidths ($\hat{\nu}_k/Q_k$, where Q_k is the loaded quality factor for the k mode). While the above criteria are necessary for efficient four-wave mixing between this set of cavity modes, they are not sufficient. In particular, as four-wave mixing can occur across multiple sets of modes simultaneously, another important factor in device design is that all other signal and idler mode sets do not simultaneously realize frequency and phase matching [21]. For example, close-to-pump OPO [33] has been a major competitive process for widely separated OPO when the device exhibits anomalous dispersion around the pump. In brief, we require the device dispersion to be such that only a single set of widely spaced signal, idler, and pump modes be phase- and frequency-matched.

Achieving such conditions can be especially challenging at visible wavelengths due to the increased dispersion of the constituent materials. The bottom panel of Fig. 1(c) summarizes the first main challenge that our design space must address, which is the strong dispersion associated with Si_3N_4 in the visible, as quantified by its group velocity dispersion (GVD), which at 600 nm (500 THz) is many times the values at 1500 nm (200 THz). Other common microresonator OPO materials like SiO_2 , AlN, and MgF_2 exhibit similar trends, although the problem is most acute for Si_3N_4 . A second challenge is how flexible the OPO design is in reaching wavelengths of interest. Ideally, we would prefer a design in which small changes in the pump frequency can result in large changes in the generated signal and idler frequencies, as schematically depicted in Fig. 1(b). Such a design would enable a broad range of output frequencies to be accessed from the narrow tuning ranges available, for example, from distributed feedback or distributed Bragg reflector pump lasers. We note that the full desired spectral range does not necessarily need to be covered within one device (as multiple devices can be fabricated on the same chip in parallel). As a result, variations in the device's in-plane geometry (ring width and ring radius) can be considered, but the device layer thickness, which is more difficult to systematically control across a chip, should ideally remain the same.

We perform a search through parameter space to determine a Si_3N_4 microring geometry with three dispersion characteristics to satisfy the above criteria: (1) phase- and frequency-matching of a single set of widely separated modes, with the signal in the visible and the idler in the infrared; (2) normal dispersion around the pump to eliminate the possibility of close-to-pump OPO in which phase-matching is mediated by nonlinear frequency shifts; and (3) flexible tuning of the OPO output wavelengths. We focus our search on the ring width (RW) and thickness (H) because they are the two parameters that define the cross section of the microring [Fig. 2(a)] and have the strongest influence on the resonator dispersion. In Fig. 2(b), we show the results of such a search. Here, we first consider the azimuthal mode numbers (m) and the corresponding simulated frequencies ($\hat{\nu}_m$) of TE1 modes using the finite-element method for a device with ring radius (RR) of 25 μm [corresponding free spectral range (FSR), of 0.9 THz], $H = 500$ nm, and $RW = 825$ nm. For each configuration that satisfies phase matching (i.e., $m_s + m_i - 2m_p = 0$), the frequency mismatch is plotted. When the pump laser is at $\nu_p = 385$ THz, while the pump is situated in normal dispersion, no modes are frequency and phase matched for OPO. When the pump laser is situated below 385 THz, the conditions for widely separated OPO start to become fulfilled, with the pump remaining in normal dispersion while only a single pair of widely separated modes is frequency matched. The span (separation between the signal and idler mode frequencies) decreases as the pump frequency decreases, and the signal mode frequency moves from about 525 THz to 425 THz. For the widest OPO, the span is ≈ 273 THz, with the signal predicted to be in the green.

As noted above, with this design, all of the aforementioned pump frequencies are in the normal dispersion regime; that is, $\hat{\nu}_s + \hat{\nu}_i - 2\hat{\nu}_p < 0$ when $\hat{\nu}_s$ and $\hat{\nu}_i$ are close to $\hat{\nu}_p$. Such dispersion prohibits close-to-pump OPO because any Kerr shift further decreases this frequency mismatch (more negative for OPO) when pump power is injected into the cavity. Therefore, we expect that our visible-infrared OPO devices should be free from competition due to close-to-pump OPO. Finally, we note that in Fig. 2, the

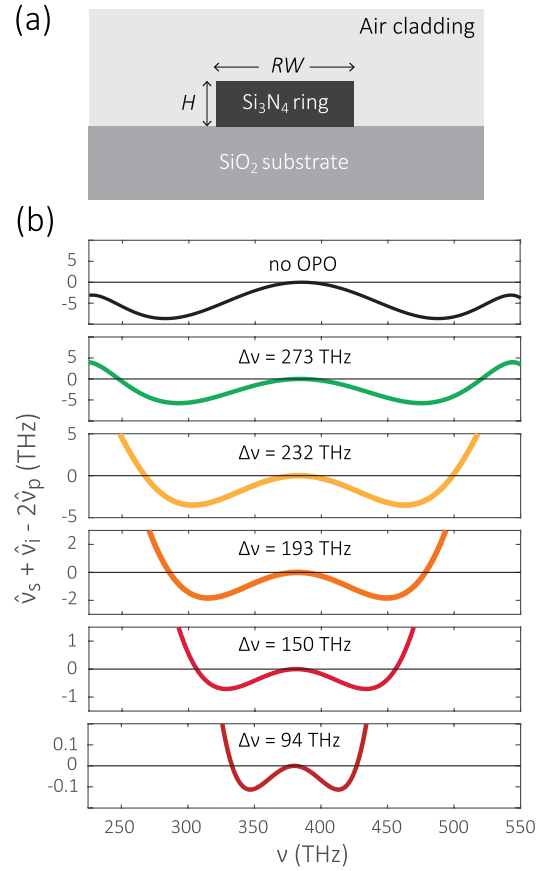


Fig. 2. Dispersion design for visible light generation. (a) Cross section view of the device shows two geometric parameters, ring width (RW), and film thickness/height (H) that are critical for dispersion engineering. (b) Simulation shows the frequency-matching profiles that support the OPO spectral separations depicted in Fig. 1(c). Frequency mismatch (y axis) is plotted for phase matched mode sets ($m_s + m_i - 2m_p = 0$), where the pump is shifted from 380 THz (bottom) to 385 THz (top) by a step of 1 THz. In the top panel, when the pump is at 385 THz (black), the device dispersion is too large to support any OPO. When the pump is decreased to 384 THz (green), the device supports octave-spanning OPO with idler and signal at 247.5 THz and 520.5 THz, respectively. A further decrease in the pump frequency leads to a smaller frequency span with different colors for the visible wavelength signal (e.g., yellow, orange, and red). The device has a radius of 25 μm , a thickness of 500 nm, and a radius of 825 nm.

resonator geometry is kept fixed and only the pump frequency is varied (in 1 FSR steps), which results in relatively coarse jumps in OPO output signal and idler frequencies. However, we note that the device geometry itself can be varied; ultimately, it is the dispersion of the resonator relative to the pump frequency that is important. As we shall show in the upcoming sections, varying both the pump frequency and resonator geometry can lead to a finer coverage of the broad spectral range predicted in Fig. 2.

4. WIDELY SEPARATED OPO INTO THE VISIBLE

The devices are fabricated (see Supplement 1 for details) according to the design shown in Fig. 2, with nominally fixed thickness and ring radius ($H = 500$ nm, $RR = 25$ μm) while varying the ring width ($RW = 820$ nm to 830 nm). Dilute hydrofluoric acid (DHF) etching is incorporated as a key step to post-process the

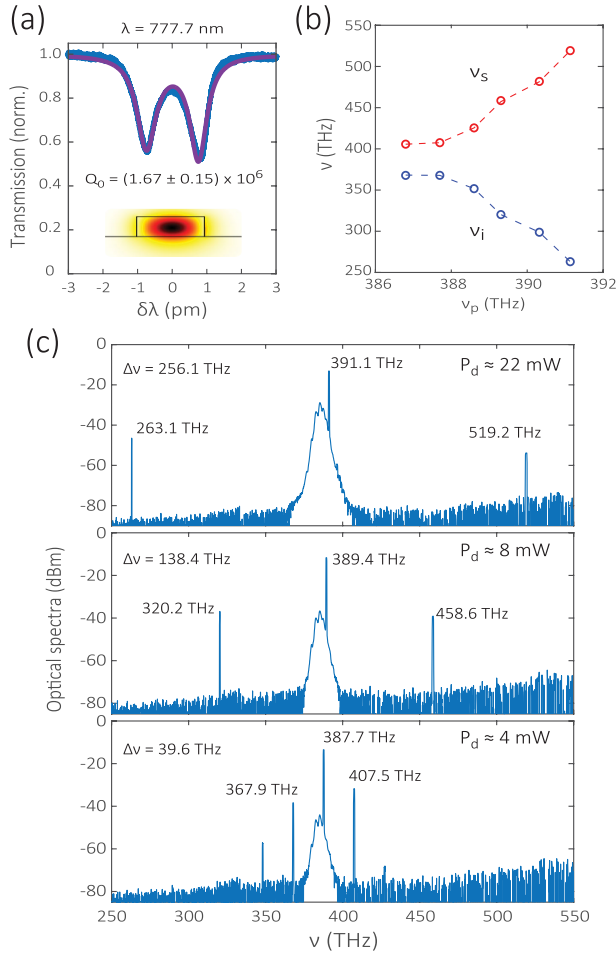


Fig. 3. Widely separated OPO in a nominal device. (a) Normalized transmission of a pump mode (fundamental transverse-electric mode, whose electric field profile is in the inset) shows an intrinsic Q of $(1.67 \pm 0.15) \times 10^6$, where the uncertainty is a one standard deviation value obtained from the fitting of the doublet resonance. (b) When the pump frequency shifts by ≈ 5 THz, the signal (red) and idler (blue) frequencies shift by 123 THz and 113 THz, respectively. The ratio of the signal/idler spectral tuning to that of pump is $\approx 26:1$. (c) Three optical spectra are shown with a pump frequency of 391.1 THz, 389.4 THz, and 387.7 THz, from top to bottom, respectively. In general, the required pump power dropped into the cavity is larger when OPO span is larger. The spectra are clean without any noise or competitive processes. In the bottom spectrum, a second pair of OPO sidebands emerges and is much weaker (≈ 20 dB) than the primary pair, and is commonly observed for OPO that is close to pump. The device has a radius of $25 \mu\text{m}$, a thickness of 500 nm, and a nominal ring width of 826 nm. The resonator free spectral range is ≈ 0.9 THz.

devices and achieve fine control of geometry at the sub-nanometer level, which in turn controls frequency and phase matching of the resonator modes. Moreover, in some cases, DHF etching improves the modes' optical quality factors. After fabrication, the devices are characterized as a function of ν_p near the simulated near-infrared frequencies around 385 THz. For example, the characterization of widely separated OPO in a device with nominal RW of 826 nm is shown in Fig. 3.

The pump mode has intrinsic Q in the range of $1 \times 10^6 - 2 \times 10^6$ and loaded $Q \approx 1 \times 10^6$. We show in Fig. 3(a), for example, a pump mode at 385.8 THz (777.7 nm), which is a fundamental transverse-electric mode (TE1) whose simulated field profile is

shown in the inset. The resonance doublet is likely due to backscattering resulting from sidewall roughness, and seems to have a random amplitude in our devices. The output OPO spectra are recorded by an optical spectrum analyzer as the pump is tuned over modes that support widely separated OPO with normal dispersion around the pump, whose frequency is adjusted between 387 THz and 391 THz [Fig. 3(b)]. When the pump frequency is > 391 THz, no widely separated OPO is observed. When the pump frequency is at 391 THz, the OPO device has its widest span of 256.1 THz [the top panel of Fig. 3(c)]. The signal is at 519.2 THz (577.8 nm), which is yellow in color, and the idler is at 254.1 THz (1140 nm) in the infrared. A further decrease in the pump frequency shifts the signal to red at 458.6 THz (654.1 nm) and then toward the near-infrared at 407.5 THz (736.2 nm), with the corresponding idler shifting from within the infrared at 320.2 THz (936.9 nm) to the near-infrared at 367.9 THz (815.4 nm), as shown in the bottom two panels of Fig. 3(c).

With this device, a mere ≈ 5 THz pump shift leads to a 123 THz shift of the signal and a 113 THz shift of the idler. Such large amplification in the output tuning range relative to the pump tuning range comes from the large dispersion of the nanophotonic resonator in the targeted frequency matching bands, and is particularly useful when wide spectral coverage is needed. In the next section, we will describe how finer steps in this spectral coverage can be achieved.

The required pump power (P_d), specified in Fig. 3(c), has a dependence on the OPO span. $P_d = P(1 - T)$ represents the pump power that is coupled into the microring, where P is the input pump power in the waveguide and T is the normalized cavity transmission of the pump laser mode. In the top panel, for example, an OPO spanning 256.1 THz requires a pump power of $P \approx 42$ mW in the waveguide, of which $P_d \approx 22$ mW is dropped into the microring to excite the OPO above threshold. In the middle and bottom panel, where the OPO span is 54% and 15% of the widest span, the required dropped power is 36% and 18% of that in the top panel. Such power dependence may come from lower Q of the cavity resonances at higher frequencies.

5. LIGHT GENERATION FROM RED TO GREEN

The wavelengths at which light is generated are very sensitive to the device geometry because of the large amplification of the frequency span relative to the pump detuning from its nominal position. As shown in the previous section, even a change in pump mode of one free spectral range (FSR ≈ 0.9 THz) leads to a > 20 THz change in the frequency of the visible signal. Similarly, a small change in device dimension, even on the order of 1 nm, can lead to a different color of light generated in the visible band. In this section, we will focus on how we can use this dispersion sensitivity alongside the previously used pump tuning to more finely cover the very larger range of OPO output frequencies possible in this platform. While each of our devices is fabricated with its own bus waveguide, we note that multiple individually addressable devices can be fabricated with the same bus waveguide, as has been shown, for example, for second harmonic generation [34].

In Fig. 4(a), we collect the pump, signal, and idler frequencies from different pumping modes in six devices with ring widths from 824 nm to 830 nm. We can see that within a 5 THz pump scan in the near-infrared (violet symbols), the OPO outputs of these devices taken together cover > 270 THz, spanning from the infrared and near-infrared to the visible, and exceeds (by nearly

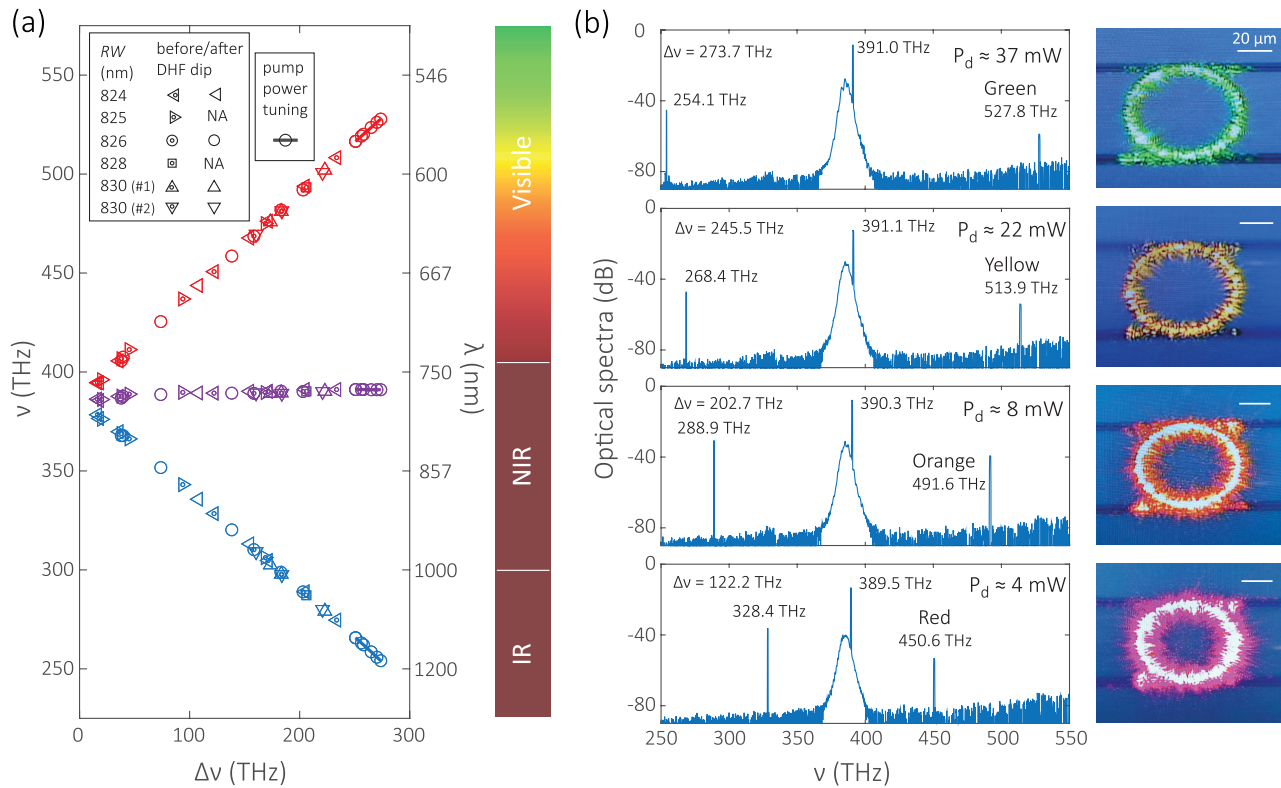


Fig. 4. OPO output light from red to green. (a) Collection of signal (red), pump (violet), and idler (blue) frequencies plotted versus the OPO span ($\Delta\nu$) for a series of devices in which the geometry (and hence, dispersion) is slightly varied. The pump laser is scanned from 386 THz to 391 THz, and its span in use is only 5 THz. The OPO signal frequencies span >130 THz, corresponding to a 26-times amplification. This figure shows data from six devices with ring widths from 824 nm to 830 nm before and after a dilute hydrofluoric acid (DHF) dip. The DHF dip isotropically removes <1 nm of Si_3N_4 , which enables the corresponding tuning of the OPO output wavelengths with a resolution beyond what we achieve through lithography and dry etching alone. The overall frequency span covers red, orange, yellow, and green signal wavelengths. In particular, OPO frequencies with $\Delta\nu$ from 256.1 THz to 273.7 THz are accessed by pump power tuning (Fig. 5), in a device with nominal RW of 826 nm after DHF dip. (b) Representative OPO spectra for signal output light in the green at 527.8 THz (568.4 nm), yellow at 513.9 THz (583.7 nm), orange at 491.6 THz (610.3 nm), and red at 450.6 THz (665.8 nm) from top to bottom, respectively. The green trace corresponds to the widest OPO achieved by pump power tuning in (a). The coupling of signal (visible) light is 10 dB–20 dB smaller than the coupling of idler (near infrared or infrared) light because of the evanescent-coupling nature of the waveguide. Optical microscope images (with illumination) show the corresponding colors that are generated. The scale bars represent 20 μm in these four images.

20 THz) the widest span shown in the previous section. The tuning of the signal and idler frequencies, although still discrete, is much finer in step than that of the single device shown in Fig. 3(b). In particular, this set of devices covers >130 THz of the visible band, including red, orange, yellow, and green colors [see the right color-bar in Fig. 4(a)], and the average step in frequency tuning for the signal is a few THz, compared to the >20 THz step shown in the previous section.

We next present four optical spectra showing the generation of green, yellow, orange, and red light in Fig. 4(b). In each case, the OPO spectrum shows no noise or competitive nonlinear processes, and its color is confirmed by optical microscope images when the device is in operation, showing red, orange, yellow, and green light generated in the microring. In particular, in a device with $RW = 826$ nm, when the pump mode is at 391.0 THz (the top panel), we observe the widest OPO with a span of 273.7 THz, which is very close to the simulated value (273 THz). The pump mode frequency is ≈ 7 THz larger than the simulation (384 THz), which is likely due to a combination of uncertainty in the refractive index model chosen for Si_3N_4 and in the fidelity of the fabricated device dimensions relative to design. This octave-spanning

OPO has a 527.8 THz (568.4 nm) signal and a 254.1 THz (1181 nm) idler.

We note that the threshold power increases from a few milliwatts to a few tens of milliwatts as the OPO output signal and idler becomes more widely separated [Figs. 3(c) and 4(b)]. It is likely due to a decrease in optical quality factors of the signal and/or idler modes. A rough estimate assuming Q values around 10^5 and 10^6 yields threshold powers of 28 mW and 2.8 mW, respectively. See Supplement 1 for details.

6. POWER TUNING: FROM MULTIPLE FSRs TO 1 FSR

The ability to realize continuous spectral coverage would complement the demonstration above of broad spectral coverage using the widely separated OPO process. The broad coverage is made possible by the dispersion properties of the resonator, which results in an amplification of the signal tuning range relative to the pump laser tuning range of $\approx 26:1$ [Fig. 4(a)]. Of course, the resonant nature of the device is such that the pump laser is not tuned continuously, but instead in jumps across different pump modes separated by the resonator FSR ≈ 0.9 THz. As a result,

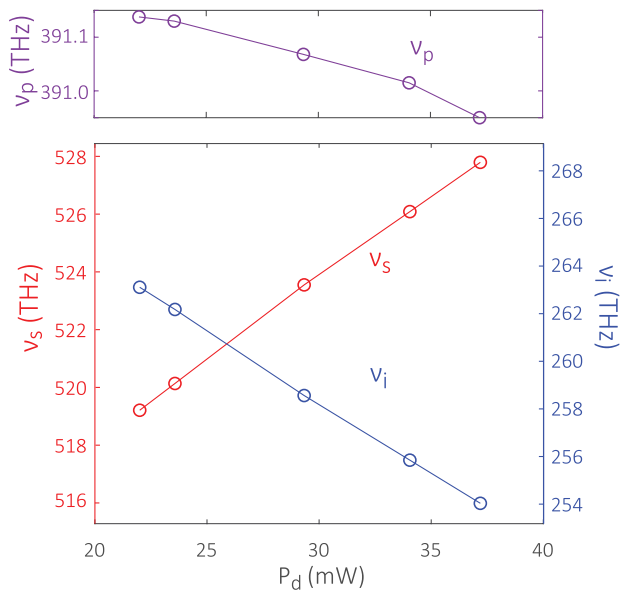


Fig. 5. Tuning of OPO frequencies with pump power. When the dropped pump power [$P_d = P(1 - T)$, where P is the laser power in the waveguide and T is the normalized cavity transmission of the pump mode that can be adjusted by laser-cavity detuning] increases from 22 mW to 37 mW, the pump frequency (ν_p) is adjusted to follow the thermo-optical shift of the pump mode.

the output spectral coverage, though broad in overall extent, is sampled with both signal and idler frequencies varying in jumps of multiple FSRs, as shown in Fig. 4(a) when both the pump frequency tuning and varying geometric dispersion are employed. In comparison, larger devices used in other OPO works in the infrared [8,13,15,16] obtain a finer step in output frequency. In this section, we show that we can achieve 1 FSR tuning steps for the signal and idler in the visible and infrared bands, respectively, by shifting one pump mode continuously through pump power tuning.

An example of this coverage is shown in Fig. 5. This device generates green light, as shown in the top panels of Figs. 3(c) and 4(b). The OPO frequencies depend on the pump power dropped into the microring (P_d), which results in a thermo-optical shift that linearly depends on P_d . We plot the pump (violet), signal (red), and idler (blue) frequencies versus P_d in Fig. 5. When P_d is 22 mW, the idler is at 263.1 THz and signal is at 519.2 THz [the top panel of Fig. 3(c)]. When P_d increases to 37 mW, the idler frequency decreases to 254.1 THz and signal frequency increases to 527.8 THz [the top panel of Fig. 4(b)]. The visible frequency shifts by 8.6 THz, while the pump frequency shifts by <0.2 THz. Therefore, this type of thermo-optic tuning method can be used to improve the spectral coverage in the visible band, bringing the multiple-FSR jumps down to about 1 FSR. Going forward, further improvement in the output tuning resolution may require using larger devices with smaller FSRs [8,13,20], but it will come at the cost of increased threshold power and also an increased chance of competing or additional four-wave mixing processes (for example, clusters of phase- and frequency-matched modes). The dispersion profile also must be adjusted and validated for larger devices.

7. DISCUSSION

In this section, we outline some of the major challenges that must be addressed to make the devices we have demonstrated functional for applications; that is, using widely separated OPO in Si_3N_4 as a flexible platform to realize on-chip visible laser light sources. The challenges include:

- **Wavelength coverage deeper into the visible.** In this work, we have shown the generation of light up to 527.8 THz, covering red, orange, yellow, and part of green. However, there are several applications for which access to higher frequencies, including the blue and violet, would be desirable. Some additional wavelength coverage can be provided using the dispersion engineering approach shown in this work, but it will be challenging to directly extend this same approach to reach blue, cyan, and violet, where the OPO signal-idler separation would reach up to two to three octaves. Overcoming this challenge will require novel designs for dispersion and waveguide-resonator coupling, while facing potentially increased material loss.

- **Output power.** The output visible power in current devices is limited to between 30 dB and 40 dB below the pump power, which is clearly not large enough for applications. There are two major reasons why the power is low. The first is the challenge associated with efficient resonator-waveguide coupling, where we can see from Fig. 4(b) that idler light (with longer wavelength and hence improved spatial overlap between the waveguide and resonator modes) is coupled 10 dB to 15 dB better than the signal light. The coupling of visible light can be optimized by appropriately designed pulley couplers [18]. Such couplers must be designed for specific wavelength bands, and universal coupling across broad spectra, particularly for short wavelengths, is very challenging due to the required corresponding small dimensions. In addition to this coupling issue, we note that at higher conversion efficiency levels, a clearer physical understanding of the pump depletion level to accurately predict both the intracavity and external signal/idler powers is needed. Finally, our basic frequency-matching design is centered around a regime in which Kerr frequency shifts due to self- and cross-phase modulation are limited. Depending on the application, one may instead seek to operate in a higher pump power regime (to enable higher absolute output powers); in that case, the Kerr shifts must be included in the design.

- **Pump laser integration.** Currently, we use a commercial fiber-coupled external cavity tunable diode laser at 780 nm to pump the devices. As noted earlier, there are several paths to more compact and integrated pumping solutions, including the use of commercial DFB and DBR laser solutions, hybrid integration of compact gain/laser chips [22,23] to create full OPO modules, and heterogeneous integration of III–V gain with Si_3N_4 photonics [24–26].

- **Wavelength tunability.** The level of wavelength tuning needed depends on the application. We have shown in this work that we can access a broad range of output wavelengths—between 568 nm and 1180 nm—by varying the pump wavelength and device geometry, suggesting the ability to access a number of different spectral bands in a common photonics platform. Tuning from one output wavelength to another is discrete, however, and the finest tuning we have demonstrated is at the 1 FSR level. To move beyond this level and improve the continuity of tuning, we note that thermal tuning has been implemented in both crystalline resonators [8] and on-chip microrings [20]. Such thermal tuning,

taken together with the incorporation of many different resonator geometries (and corresponding dispersion profiles) on a common bus waveguide, may provide a first step to realizing both ultrawide wavelength coverage and fine wavelength tuning. That being said, the overall scope of the challenge is considerable and one may anticipate new advances to address the problem more completely.

8. CONCLUSION

In summary, we propose and demonstrate, for the first time to the best of our knowledge, nanophotonic OPO devices whose output frequencies (including both the signal and idler) cover a range from 527.8 THz to 254.1 THz, which encompasses the green, yellow, orange, and red parts of the visible spectrum, as well as the near-infrared and a portion of the infrared spectrum. Our OPO devices magnify the frequency tuning span of the near-infrared pump source by ≈ 25 times in the generated output frequency ranges for both the infrared idler and visible signal light. Devices whose dispersion support the widest separation in signal and idler frequencies exhibit octave-spanning OPO at <30 mW threshold power. We further show a tuning method to achieve 1 FSR output tuning steps. We believe our work is a major advance in the realization of coherent on-chip sources of visible light.

Funding. Defense Advanced Research Projects Agency (DODOS); National Institute of Standards and Technology (NIST-on-a-chip).

Acknowledgment. Authors Xiyuan Lu and Kartik Srinivasan thank Dr. Andrey Matsko for helpful discussions regarding OPO in ultra-high-Q resonators. Author Lu acknowledges support under the Cooperative Research Agreement between the University of Maryland and NIST-PML.

Disclosures. The authors declare no conflicts of interest.

See [Supplement 1](#) for supporting content.

REFERENCES

1. L. Hollberg, C. W. Oates, G. Wilpers, C. W. Hoyt, Z. W. Barber, S. A. Diddams, W. H. Oskay, and J. C. Bergquist, "Optical frequency/wavelength references," *J. Phys. B* **38**, S469–S495 (2005).
2. A. D. Ludlow, M. M. Boyd, J. Ye, E. Peik, and P. O. Schmidt, "Optical atomic clocks," *Rev. Mod. Phys.* **87**, 637–701 (2015).
3. C. Simon, M. Afzelius, J. Appel, A. Boyer de la Giroday, S. J. Dewhurst, N. Gisin, C. Y. Hu, F. Jelezko, S. Kröll, J. H. Müller, J. Nunn, E. S. Polzik, J. G. Rarity, H. De Riedmatten, W. Rosenfeld, A. J. Shields, N. Sköld, R. M. Stevenson, R. Thew, I. A. Walmsley, M. C. Weber, H. Weinfurter, J. Wrachtrup, and R. J. Young, "Quantum memories. A review based on the European integrated project 'Qubit Applications (QAP)'," *Eur. Phys. J. D* **58**, 1–22 (2010).
4. Y. Sun, K. Zhou, Q. Sun, J. Liu, M. Feng, Z. Li, Y. Zhou, L. Zhang, D. Li, S. Zhang, M. Ikeda, S. Liu, and H. Yang, "Room-temperature continuous-wave electrically injected InGaN-based laser directly grown on Si," *Nat. Photonics* **10**, 595–599 (2016).
5. R. W. Boyd, *Nonlinear Optics* (Academic, 2008).
6. G. Agrawal, *Nonlinear Fiber Optics* (Academic, 2007).
7. M. Ebrahimzadeh, M. H. Dunn, and F. Akerboom, "Highly efficient visible urea optical parametric oscillator pumped by a XeCl excimer laser," *Opt. Lett.* **14**, 560–562 (1989).
8. N. L. B. Sayson, T. Bi, V. Ng, H. Pham, L. S. Trainor, H. G. L. Schwefel, S. Coen, M. Erkintalo, and S. G. Murdoch, "Octave-spanning tunable parametric oscillation in crystalline Kerr microresonators," *Nat. Photonics* **13**, 701–706 (2019).
9. C. S. Werner, T. Beckmann, K. Buse, and I. Breunig, "Blue-pumped whispering gallery optical parametric oscillator," *Opt. Lett.* **37**, 4224–4226 (2012).
10. W. Liang, A. A. Savchenkov, J. McMillan, Z. Xie, V. S. Ilchenko, D. Seidel, C. W. Wong, A. B. Matsko, and L. Maleki, "Strongly nondegenerate resonant optical parametric oscillator," in *Nonlinear Optics* (Optical Society of America, 2013), paper NF1A.5.
11. W. Liang, A. A. Savchenkov, Z. Xie, J. F. McMillan, J. Burkhart, V. S. Ilchenko, C. W. Wong, A. B. Matsko, and L. Maleki, "Miniature multi-octave light source based on a monolithic microcavity," *Optica* **2**, 40–47 (2015).
12. A. B. Matsko, A. A. Savchenkov, S.-W. Huang, and L. Maleki, "Clustered frequency comb," *Opt. Lett.* **41**, 5102–5105 (2016).
13. S. Fujii, S. Tanaka, M. Fuchida, H. Amano, Y. Hayama, R. Suzuki, Y. Kakinuma, and T. Tanabe, "Octave-wide phase-matched four-wave mixing in dispersion engineered crystalline microresonators," *Opt. Lett.* **42**, 3149 (2019).
14. I. Breunig, "Three-wave mixing in whispering gallery resonators," *Laser Photon. Rev.* **10**, 569–587 (2016).
15. N. L. B. Sayson, K. E. Webb, S. Coen, M. Erkintalo, and S. G. Murdoch, "Widely tunable optical parametric oscillation in a Kerr microresonator," *Opt. Lett.* **42**, 5190–5193 (2017).
16. S. Fujii, T. Kato, R. Suzuki, and T. Tanabe, "Third-harmonic blue light generation from Kerr clustered combs and dispersive waves," *Opt. Lett.* **42**, 2010–2013 (2017).
17. J. H. Chen, X. Shen, S. J. Tang, Q. T. Cao, Q. Gong, and Y. F. Xiao, "Microcavity nonlinear optics with an organically functionalized surface," *Phys. Rev. Lett.* **123**, 173902 (2019).
18. X. Lu, G. Moille, Q. Li, D. A. Westly, A. Rao, S.-P. Yu, T. C. Briles, S. B. Papp, and K. Srinivasan, "Efficient telecom-to-visible spectral translation using silicon nanophotonics," *Nat. Photon.* **13**, 593–601 (2019).
19. A. W. Bruch, X. Liu, J. B. Surya, C.-L. Zou, and H. X. Tang, "On-chip $\chi^{(2)}$ microring optical parametric oscillator," *Optica* **6**, 1361–1366 (2019).
20. Y. Tang, Z. Gong, X. Liu, and H. Tang, "Widely separated optical Kerr parametric oscillation in AlN microrings," *Opt. Lett.* **45**, 1124–1127 (2020).
21. X. Lu, G. Moille, A. Singh, Q. Li, D. A. Westly, A. Rao, S.-P. Yu, T. C. Briles, S. B. Papp, and K. Srinivasan, "Milliwatt-threshold visible-telecom optical parametric oscillation using silicon nanophotonics," *Optica* **6**, 1535–1541 (2019).
22. B. Stern, X. Ji, Y. Okawachi, A. L. Gaeta, and M. Lipson, "Battery-operated integrated frequency comb generator," *Nature* **562**, 401–405 (2018).
23. A. S. Raja, A. S. Voloshin, H. Guo, S. E. Agafonova, J. Liu, A. S. Gorodnitskiy, M. Karpov, N. G. Pavlov, E. Lucas, R. R. Galiev, A. E. Shitikov, J. D. Jost, M. L. Gorodetsky, and T. J. Kippenberg, "Electrically pumped photonic integrated soliton microcomb," *Nat. Commun.* **10**, 680 (2019).
24. C. Xiang, W. Jin, J. Guo, J. D. Peters, M. J. Kennedy, J. Selvidge, P. A. Morton, and J. E. Bowers, "Narrow-linewidth III-V/Si/Si₃N₄ laser using multilayer heterogeneous integration," *Optica* **7**, 20–21 (2020).
25. C. Op de Beeck, B. Haq, L. Elsinger, A. Gocalinska, E. Pelucchi, B. Corbett, G. Roelkens, and B. Kuyken, "Heterogeneous III-V on silicon nitride amplifiers and lasers via microtransfer printing," *Optica* **7**, 386–393 (2020).
26. H. Park, C. Zhang, M. A. Tran, and T. Komljenovic, "Heterogeneous silicon nitride photonics," *Optica* **7**, 336–337 (2020).
27. D. J. Moss, R. Morandotti, A. L. Gaeta, and M. Lipson, "New CMOS-compatible platforms based on silicon nitride and Hydex for nonlinear optics," *Nat. Photonics* **7**, 597–607 (2013).
28. Y. Okawachi, K. Saha, J. S. Levy, Y. H. Wen, M. Lipson, and A. L. Gaeta, "Octave-spanning frequency comb generation in a silicon nitride chip," *Opt. Lett.* **36**, 3398–3400 (2011).
29. Q. Li, T. C. Briles, D. A. Westly, T. E. Drake, J. R. Stone, B. R. Ilic, S. A. Diddams, S. B. Papp, and K. Srinivasan, "Stably accessing octave-spanning microresonator frequency combs in the soliton regime," *Optica* **4**, 193–203 (2017).

30. M. Karpov, M. H. Pfeiffer, J. Liu, A. Lukashchuk, and T. J. Kippenberg, "Photonic chip-based soliton frequency combs covering the biological imaging window," *Nat. Commun.* **9**, 1146 (2018).
31. Q. Li, M. Davanço, and K. Srinivasan, "Efficient and low-noise single-photon-level frequency conversion interfaces using silicon nanophotonics," *Nat. Photonics* **10**, 406–414 (2016).
32. Y. Zhao, X. Ji, B. Y. Kim, P. S. Donvalkar, J. K. Jang, C. Joshi, M. Yu, C. Joshi, R. R. Domenegueti, F. A. S. Barbosa, P. Nussenzveig, Y. Okawachi, M. Lipson, and A. L. Gaeta, "Visible nonlinear photonics via high-order-mode dispersion engineering," *Optica* **7**, 135–141 (2020).
33. T. J. Kippenberg, S. Spillane, and K. J. Vahala, "Kerr-nonlinearity optical parametric oscillation in an ultrahigh-Q toroid microcavity," *Phys. Rev. Lett.* **93**, 083904 (2004).
34. J. B. Surya, X. Guo, C.-L. Zou, and H. X. Tang, "Control of second-harmonic generation in doubly resonant aluminum nitride microrings to address a rubidium two-photon clock transition," *Opt. Lett.* **43**, 2696–2699 (2018).